remote sensing

MDPI

Article

Simulation and Assessment of the Capabilities of Orbita Hyperspectral (OHS) Imagery for Remotely Monitoring Chlorophyll-a in Eutrophic Plateau Lakes

Runfei Zhang [1], Zhubin Zheng [1,*], Ge Liu [2], Chenggong Du [3], Chao Du [1], Shaohua Lei [4], Yifan Xu [5], Jie Xu [4], Meng Mu [4], Shun Bi [4] and Jianzhong Li [1]

1 School of Geography and Environmental Engineering, Gannan Normal University, Ganzhou 341000, China; zhangrunfei98@gmail.com (R.Z.); chao.du@gnnu.edu.cn (C.D.); lijianzhong@gnnu.edu.cn (J.L.)
2 The Northeast Institute of Geography and Agricultural Ecology, Chinese Academy of Sciences, Changchun 130102, China; liuge@iga.ac.cn
3 Jiangsu Collaborative Innovation Center of Regional Modern Agriculture & Environmental Protection, Huaiyin Normal University, Huai'an 223000, China; ducg1023@163.com
4 Key Laboratory of Virtual Geographic Environment, Ministry of Education, College of Geographic Science, Nanjing Normal University, Nanjing 210023, China; 171301035@stu.njnu.edu.cn (S.L.); 171301036@stu.njnu.edu.cn (J.X.); 161301037@stu.njnu.edu.cn (M.M.); 161302127@stu.njnu.edu.cn (S.B.)
5 State Key Laboratory of Hydrology-Water Resources and Hydraulic Engineering, Nanjing Hydraulic Research Institute, Nanjing 210029, China; xuyf@nhri.cn
* Correspondence: zhengzhubin@gnnu.edu.cn

Citation: Zhang, R.; Zheng, Z.; Liu, G.; Du, C.; Du, C.; Lei, S.; Xu, Y.; Xu, J.; Mu, M.; Bi, S.; et al. Simulation and Assessment of the Capabilities of Orbita Hyperspectral (OHS) Imagery for Remotely Monitoring Chlorophyll-a in Eutrophic Plateau Lakes. *Remote Sens.* **2021**, *13*, 2821. https://doi.org/10.3390/rs13142821

Academic Editors: Jiayi Pan, Bo Huang, Hongsheng Zhang and Adam T. Devlin

Received: 27 May 2021
Accepted: 15 July 2021
Published: 18 July 2021

Abstract: The chlorophyll-a (Chl-a) concentration of eutrophic lakes fluctuates significantly due to the disturbance of wind and anthropogenic activities on the water body. Consequently, estimation of the Chl-a concentration has become an immense challenge. Due to urgent demand and rapid development in high-resolution earth observation systems, it has become crucial to assess hyperspectral satellite imagery capabilities on inland water monitoring. The Orbita hyperspectral (OHS) satellite is the latest hyperspectral sensor with both high spectral and spatial resolution (2.5 nm and 10 m, respectively), which could provide great potential for remotely estimating the concentration of Chl-a for inland waters. However, there are still some deficiencies that are mainly manifested in the Chl-a concentration remote sensing retrieval model assessment and accuracy validation, as well as signal-to-noise ratio (SNR) estimation of OHS imagery for inland waters. Therefore, the radiometric performance of OHS imagery for water quality monitoring is evaluated in this study by comparing different atmospheric correction models and the SNR with several remote sensing images. Several crucial findings can be drawn: (1) the three-band model ((1/B15-1/B17)B19) developed by OHS imagery is most suitable for estimating the Chl-a concentration in Dianchi Lake, with the root-mean-square error (RMSE) and the mean absolute percentage error (MAPE) of 15.55 μg/L and 16.31%, respectively; (2) the applicability of the FLAASH (Fast Line-of-sight Atmospheric Analysis of Spectral Hypercubes) atmospheric correction model for OHS imagery in a eutrophic plateau lake (Dianchi Lake) was better than the 6S (Second Simulation of Satellite Signal in the Solar Spectrum) model, and QUAC (Quick Atmospheric Correction) model, as well as the dark pixel method; (3) the SNR of the OHS imagery was similar to that of Hyperion imagery and was significantly higher than SNR of the HSI imagery; (4) the spatial resolution showed slight influence on the SNR of the OHS imagery. The results show that OHS imagery could be applied to remote sensing retrieval of Chl-a in eutrophic plateau lakes and presents a new tool for dynamic hyperspectral monitoring of water quality.

Keywords: orbita hyperspectral imagery; Dianchi Lake; Chlorophyll-a; atmospheric correction; signal-to-noise ratio

1. Introduction

Chlorophyll-a (Chl-a) is a crucial parameter which impacts the watercolor of inland lake water, and is a vital indicator measuring the eutrophication degree of lake water [1,2]. The nutrients transported by Chl-a reduce the spread of light through a water column and affect the natural operation of the entire aquatic ecosystem. Therefore, accurate prediction of Chl-a concentration and its spatiotemporal distribution pattern is of great significance to the protection of lake ecosystems and the improvement of water quality monitoring capabilities, and is the basis of water environment remote sensing monitoring and evaluation. Precise prediction of Chl-a concentration is also the focus and challenge of watercolor remote sensing [3–6].

Dianchi Lake is the largest freshwater lake in Southwest China and the sixth-largest freshwater lake in China. It is an important drinking water source for residents, one of many important habitats for migratory birds, and an essential part of the wetland ecosystem. Due to continuous urbanization, Dianchi Lake has become a "sewage bucket" for domestic sewage, industrial wastewater, and agricultural sewage. The eutrophication of water bodies has become increasingly serious, and this lake has matured into a typical representative of eutrophic lakes in the country. The pollution of the Dianchi Lake has caused an undesirable evolution of the biological population structure and aquatic ecosystems. The resulting cyanobacterial blooms have greatly impacted the production and life of local inhabitants and are a major threat to the ecological environment and biological diversity [7–10]. Hence, it is particularly important to judiciously monitor the eutrophication level of Dianchi Lake and consider Dianchi Lake as a chief target for eutrophication control.

This eutrophic plateau lake is greatly affected by the disturbance of wind and anthropogenic activities, making it difficult to retrieve the Chl-a concentration. Moreover, most previous studies focused on multi-spectral remote estimation [11–16], with few studies for hyperspectral inversion models in eutrophic plateau lake existing [17]. O'Reilly et al. [18] used the blue-green band ratio model to estimate the concentration of Chl-a in the ocean based on Sea-Viewing Wide Field-of-View Sensor (SeaWiFS) images. Gurlin et al. [19] proposed the near-infrared and red band ratio model and applied it to Moderate Resolution Imaging Spectroradiometer (MODIS) and Medium Resolution Imaging Spectrometer (MERIS) images to estimate the Chl-a concentration. Matthews et al. [20] utilized the maximum peak height algorithm to estimate the Chl-a concentration of inland waters. Liu et al. [21] executed semi-analytical algorithms to retrieve the Chl-a concentration of various lakes based on Ocean and Land Color Instrument (OLCI) images. Ioannou et al. [22] implemented neural network algorithms to predict the Chl-a concentration and used them on MODIS images. Due to the complexity of the optical properties of water bodies and the diverse performance of each image, the Chl-a concentration retrieval accuracy was significantly different. Hence, the current dilemmas mainly include the following: (1) the accuracy of multi-spectral inversion models for eutrophic plateau lakes needs improvement; (2) while there is less research on hyperspectral data, its inversion models results may be more accurate compared to multi-spectral data; (3) there is no research on the applicability of OHS (Orbita hyperspectral) data for eutrophic plateau lakes; (4) the problems of atmospheric correction and SNR (signal-to-noise ratio) of OHS imagery have not been resolved.

Retrieving the concentration of Chl-a in eutrophic plateau lakes using the OHS image was a major challenge. This challenge was mainly addressed because OHS imagery has rarely been used in the field of remote sensing and the uncertainty of OHS imagery for Chl-a concentration estimation is still unknown. OHS imagery is an imaging product integrating high spectral resolution, high spatial resolution, and high temporal resolution, and is a hyperspectral satellite with great development potential. Most existing hyperspectral imagers can no longer be used. For instance, the Hyperion hyperspectral sensor mounted on the EO-1 (Earth Observing-1) satellite platform and the AVIRIS (Airborne Visible Infrared Imaging Spectrometer) hyperspectral imager positioned on the ER-2 (European Remote sensing-2) aircraft platform has been terminated; the HJ-1 HSI (Hyperspectral Imager) and

the images produced by the CHRIS (Compact High-Resolution Imaging Spectrometer) sensor mounted on the PROBA (Project for On-Board Autonomy) satellite cannot be used due to stripe noise. In addition, the Hyperspectral Precursor of the Application Mission (PRISMA) satellite launched in March 2019 offers great potential for hyperspectral monitoring of water quality in inland lakes, but its imaging products have certain uncertainties [23]; the DESIS (DLR Earth Sensing Imaging Spectrometer) hyperspectral sensor installed on the International Space Station can play a crucial role in monitoring coastal and inland water bodies, but has difficulty monitoring small-scale lake water bodies due to the low spatial resolution [24]; the HISUI (Hyperspectral Imager Suite) hyperspectral instrument onboard the ALOS-3 (Advanced Land Observing Satellite-3) satellite was successfully launched in December 2019, but the quality of its imaging products and its ability to monitor inland water bodies are still unknown. Therefore, the emergence of the OHS satellite provides opportunities for hyperspectral remote sensing monitoring of small-scale inland lakes. This study assesses the performance of OHS imagery for remote sensing inversion of water quality parameters from the perspective of inland lake water quality monitoring.

This study aims to quantitatively reveal and analyze the spatial pattern of Chl-a concentration in eutrophic plateau lakes using OHS imagery in Dianchi Lake, with the following main objectives: (1) Develop a model based on the novel OHS imagery for Chl-a remote sensing retrieval in eutrophic plateau lakes; (2) Explore the applicability and feasibility of OHS imagery for monitoring Chl-a concentration in eutrophic plateau lakes.

2. Materials and Methods

2.1. Study Area

Located on the Yunnan–Guizhou Plateau, Dianchi Lake (102°31′E~102°56′E, 24°32′N ~25°17′N, Figure 1) is the largest freshwater lake in Yunnan Province and the largest plateau lake in the southwest region of China, with an altitude of 1886 m, a lake area of 330 km^2, and an average water depth of 5 m. It is a typical plateau lake with eutrophication and is significantly affected by wind and human activities. Dianchi Lake is a vital source of drinking water for local inhabitants. It also functions as a reservoir for industry and agriculture, flood control, shipping, tourism, aquaculture, hydroelectric power generation, and meteorological regulation, and plays a critical role in the development of Kunming's social economy. Over recent decades, the rise of industry, rapid social and economic development, and constant population growth around Dianchi Lake have caused more and more pollutants access to Dianchi Lake, resulting in increasingly severe eutrophication. In current years, although the water quality of Dianchi Lake has improved, it is still in Level-IV (extremely eutrophic water body according to Dianchi Lake Administration Bureau). The management and ecological restoration of Dianchi Lake is threatened.

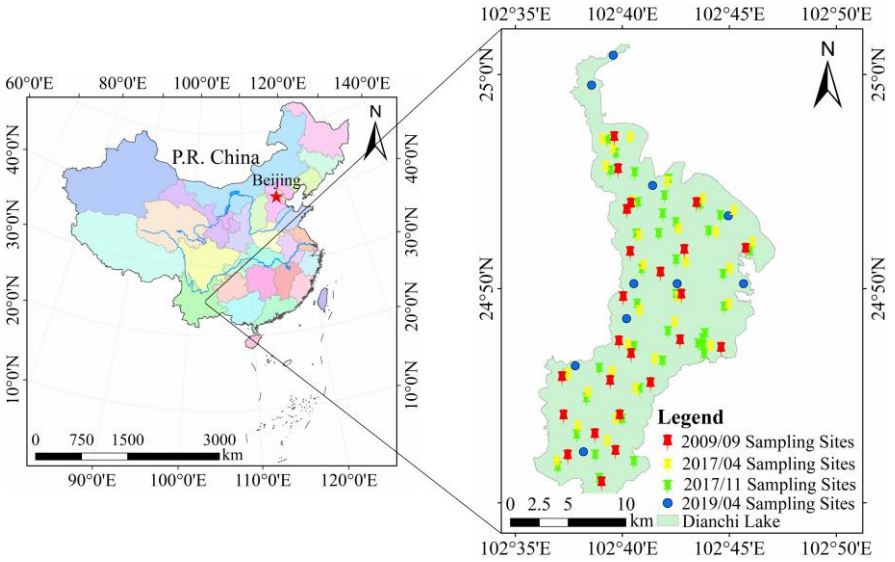

Figure 1. Dianchi Lake and sampling sites location distribution in China. The chromatic points indicate the sampling sites, and the light green area indicates Dianchi Lake. The red pushpins indicate the sampling sites in April 2009, the yellow pushpins represent the sampling sites in April 2017, the green pushpins denote the sampling points in November 2017, and the blue dots refer to the sampling points in April 2019.

2.2. Remote Sensing Images and Images Pre-Processing

Five types of imagery data were used in this study, including (1) the OHS imagery on 2 April 2019, with both high spectral and spatial resolution (2.5 nm and 10 m, respectively), a band range of 400 nm–1000 nm, and a total of 32 spectral bands [25] (Table A1), was downloaded from Zhuhai Orbita Aerospace Technology Co., Ltd. in Zhuhai, China (https://ohs.obtdata.com/, accessed on 30 May 2019); (2) Landsat-8 OLI imagery on 7 May 2019, originating from the United States Geological Survey (USGS, https://glovis.usgs.gov/, accessed on 5 June 2019); (3) Hyperion imagery on 21 May 2004, from the United States Geological Survey (USGS, https://glovis.usgs.gov/, accessed on 5 June 2019); (4) HJ-1 HSI imagery on 25 November 2014, which came from China Centre for Resources Satellite Data and Application (CRESDA, http://www.cresda.com/, accessed on 5 June 2019), and (5) Sentinel-2 MSI (Multispectral Instrument) imagery on 7 April 2019, collected from the European Space Agency (ESA, https://scihub.copernicus.eu/, accessed on 5 June 2019). Among them, OHS imagery was used for all operations in this study, and other imageries were used to estimate the SNR.

2.2.1. Radiometric Calibration

Radiometric calibration is the process of converting the digital number value (DN) of remote sensing images into top-of-atmosphere (TOA) radiance or apparent reflectance. In this study, radiometric calibration was performed using Environment for Visualizing Images (ENVI) software to convert its DN value into apparent radiance via [25,26]. First, we performed radiometric calibration on OHS imagery in this study.

$$L_e = gain \times \frac{DN}{TDIStage} + offset \quad (1)$$

where, L_e is the apparent radiance, *gain* is the gain coefficient, *offset* is the offset coefficient, and *TDIStage* is the integration series (Table A1).

2.2.2. Atmospheric Correction

Atmospheric correction eliminates and corrects the absorption or scattering of sunlight caused by the atmosphere, the reflection from the target or absorption and scattering of scattered light, and the incident light to the sensor in addition to the light from the target. Its basic algorithm is given in Equation (2) [26]. We performed atmospheric correction on OHS imagery in this study.

$$L = \left(\frac{A * \rho}{1 - \rho_e * S}\right) + \left(\frac{B * \rho_e}{1 - \rho_e * S}\right) + (L_a) \quad (2)$$

where, L is the total radiance received by the pixel at the sensor, ρ is the real surface reflectance of the pixel, ρ_e is the average surface reflectance around the pixel, S is the atmosphere spherical albedo, and L_a is the atmospheric backscattered radiance (atmospheric range radiation); A and B are two coefficients depending on atmospheric conditions and geometric conditions.

In this study, the FLAASH (Fast Line-of-sight Atmospheric Analysis of Spectral Hypercubes) model, QUAC (Quick Atmospheric Correction) model, 6S (Second Simulation of Satellite Signal in the Solar Spectrum) model, and dark pixel method were used to perform atmospheric correction on the OHS image. Among them, FLAASH is an atmospheric correction module based on the MODTRAN5 (Moderate Resolution Atmospheric Transmission) radiation transfer model, which can be applied to hyperspectral and multispectral images; QUAC model is a quick atmospheric correction method incorporated in ENVI software; 6S model is used to simulate the radiation transfer process of 0.25~4.00 μm solar reflectance wave band and is an improved version of the 5S (Simulation of Satellite Signal in the Solar Spectrum) model; dark pixel method assumes that the radiance of water body dark pixel in the infrared band is approximately 0 and the radiation received by the sensor in this band comes from atmospheric effects from which the atmospheric parameters and aerosol factors are derived. The visible bands are extrapolated and atmospherically corrected [26].

2.3. Field Measurements

Three cruise field surveys conducted on 19 to 20 September 2009, 13 to 16 April 2017, and 13 to 15 November 2017 over Dianchi Lake measured and collected remote sensing reflectance (R_{rs}) and water sample data. We collected 93 samples in 3 field surveys (Figure 1). At each station, the longitude and latitude coordinates were recorded using a Global Positioning System (GPS) receiver and roughly 1000–1500 mL surface water samples from a 50 cm water depth were collected for laboratory measurement and analysis [27,28]. In addition, we obtained the measured Chl-a concentration data collected by Dianchi Administration Bureau on 2 April 2019. Among them, 93 observation stations datasets from three field measurements (19 to 20 September 2009, 13 to 16 April 2017, and 13 to 15 November 2017) were used to develop and validate the Chl-a retrieval models; the in situ Chl-a concentration data (N = 10) of Dianchi Lake synchronized with OHS imagery (2 April 2019) were used to validate the performance of the OHS imagery retrieval results (Table 1).

Table 1. The description of field measurement data set of four cruise field surveys on 19 to 20 September 2009, 13 to 16 April 2017, 13 to 15 November 2017, and 2 April 2019.

Total Dataset	Sampling Time (YYYY/MM/DD)	Training Dataset	Validation Dataset	Usage
N = 24	2009/09/19–2009/09/20	N = 16	N = 8	Simulated OHS-based model calibration and validation
N = 30	2017/04/13–2017/04/16	N = 20	N = 10	
N = 39	2017/11/13–2017/11/15	N = 25	N = 14	
N = 10 *	2019/04/02	N = 0	N = 10	Validation of derived Chl-a from OHS imagery

* This data set originated from the Dianchi Administration Bureau and only has the in situ Chl-a concentration data synchronized with the OHS imagery but does not have the spectral reflectance data.

2.3.1. Radiometric Measurements

Spectral reflectance was measured using an ASD FieldSpec spectroradiometer. The instrument has 512 spectral channels with a spectral resolution of 1.5 nm across a spectral range of 350–1050 nm. The radiance spectra of the reference panel, water, and sky were measured using the above-water measurement method followed by the Ocean Optics Protocols [29,30]. The observation geometry with an azimuth of 135° and a nadir angle of 40° was used to avoid direct sunlight reflection on the water [30]. Ten spectra were obtained for each sampling site, from which we eliminated abnormal spectra due to occasional factors and averaged valid ones to calculate the remote sensing reflectance ($R_{rs}(\lambda)$) via the following equation [30,31] (Figure 2):

$$R_{rs}(\lambda) = \frac{\left(L_t - \rho L_{sky}\right) * R_g}{L_g \pi} \quad (3)$$

where, L_t is the measured total radiance from the water surface; ρ is the skylight reflectance received from the air–water surface, which is considered as 2.2% for calm weather, 2.5% for wind speed reaching 5 m·s^{-1}, and 2.6%–2.8% for wind speed of 10 m·s^{-1}; L_{sky} is the determined radiance of the sky; L_g is the radiance measured with the reference panel; R_g is the reflectance from the reference panel, and its value is 30%.

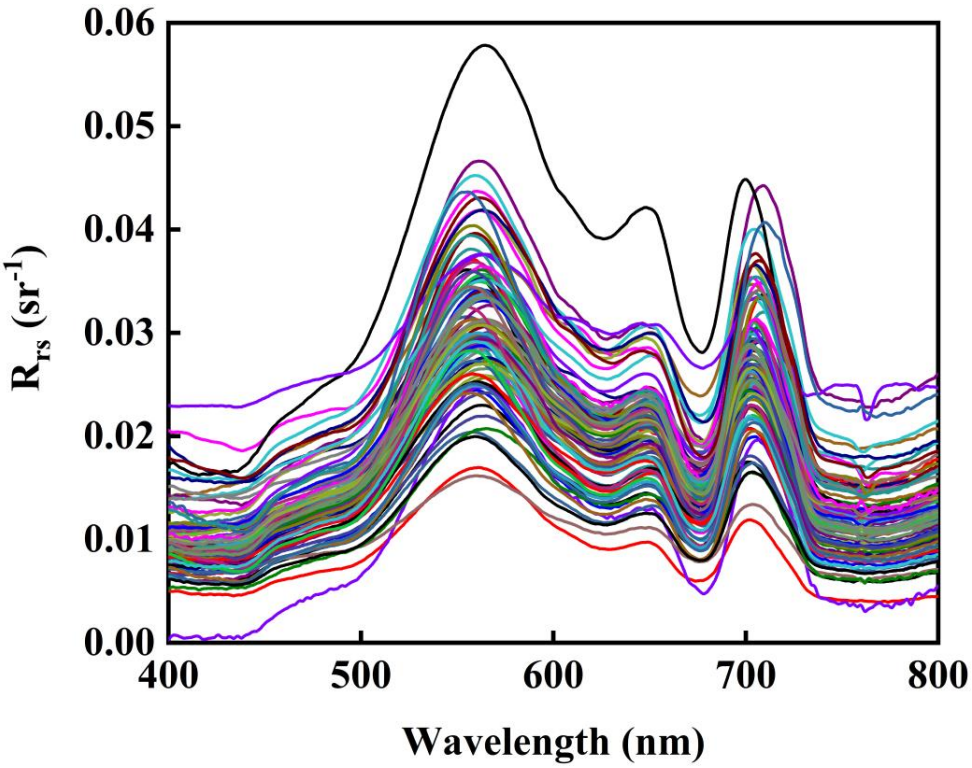

Figure 2. Spectral characteristics of field measurement sampling points. Each spectrum represents the remote sensing reflectance properties of each sampling point.

2.3.2. Water Sample Analysis

Water samples were filtered using Whatman GF/F fiberglass filters, and phytoplankton pigments were extracted in 90% hot ethanol at 80 °C. Chl-a concentration was measured using hot ethanol methods [32], that is, the concentration of Chl-a was extracted with 90% hot ethanol at 80 °C, the resulting extract was acidified with 1% dilute hydrochloric acid, and the absorbance at 665 nm and 750 nm was measured by a UV2550 spectrophotometer. The Chl-a concentration was determined using the absorbance at 665 nm and 750 nm. The concentrations of total suspended matter (TSM), organic suspended matter (OSM),

and inorganic suspended matter (ISM) were measured using detailed descriptions from American Public Health Association [33]. The water sample was filtered on a Whatman GF/F glass fiber filter and weighed according to the method of Huang [34]. The filter was then re-heated at 550 °C for 4 h to remove the organic ingredients and weighed again to determine ISM. The OSM concentration can be obtained by subtracting ISM from TSM.

2.4. Model Calibration Based on Simulated OHS Imagery

To estimate the Chl-a concentration using the OHS image, the spectral reflectance of the field measurements and the spectral response function of the OHS image were used by the atmosphere-surface scene simulation method to simulate the spectral characteristics of the in situ remote sensing reflectance to the spectral characteristics of OHS image. $R_{rs}(\lambda)$ was used to represent the remote sensing reflectance received by the water-surface reflecting sunlight and reaching the ASD sensor detector. After considering the spectral response function $f(\lambda)$, the simulation result can be derived by the following formula [35,36]:

$$R_{rs}(B_i) = \frac{\int_{\lambda_{\min}}^{\lambda_{\max}} R_{rs}(\lambda) f(\lambda) d\lambda}{\int_{\lambda_{\min}}^{\lambda_{\max}} f(\lambda) d\lambda} \quad (4)$$

where, $R_{rs}(B_i)$ denotes the simulated field-measured $R_{rs}(\lambda)$ for the i-th band of OHS image, with integration from $\lambda_{\min}$ to $\lambda_{\max}$ for the i-th band.

2.5. Signal-to-Noise Ratio Estimation

SNR is a measure of the relationship between signal and noise and is a particularly important indicator to evaluate the performance of a sensor. According to Tobler's first law of geography, adjacent features of the same kind have similar spectral characteristics, corresponding to a similar gray value in the image of the same band. The SNR of the OHS image was determined using the variance method [37,38]. However, the premise of the method must ensure that the pixels involved in the operation were homogeneous features. The central area of Dianchi Lake selected in this study was rather homogeneous, and it was assumed that their bio-optical characteristics were spatially stable.

The specific process was: (1) extracted a pure window, that is, an area with relatively homogeneous optical properties in the center of Dianchi Lake; (2) determined the average DN value and standard deviation of all pixels in the pure window; (3) the ratio of the mean value and the standard deviation was SNR of remote sensing imagery. The formula of SNR is as follows:

$$MDN = \frac{\sum DN_i}{N}. \quad (5)$$

$$S = \sqrt{\frac{\sum (DN_i - MDN)^2}{N-1}} \quad (6)$$

$$SNR = \frac{MDN}{S} \quad (7)$$

where, MDN is the mean DN value of the pixels, DN_i is the DN value of each pixel in the image of the selected area, N is the number of pixels, S is the standard deviation of the DN value of the pixels, and SNR is the signal-to-noise ratio of the OHS image.

2.6. Statistical Analysis

Statistical analyses including calculations of the mean, maximum, and minimum values, correlation analysis, and linear and non-linear regressions were performed using the Microsoft Excel software. Additionally, several metrics were used to assess the algorithm's performance and uncertainties in this study, which include (1) the Pearson correlation coefficient (r), (2) the determination coefficient (R^2), (3) the root-mean-square error (RMSE), (4) the mean absolute percentage error (MAPE), and (5) p-value that represents the significance level of the association between two variables, and was reported

to be significant ($p < 0.05$) or not significant ($p > 0.05$) with a t-test. Among them, the r and R^2 indicate the degree of correlation between the coupled data; the *RMSE* represents the difference between the predicted value and the actual value, smaller *RMSE* denotes higher prediction accuracies; and the *MAPE* is a measure of the prediction accuracy of a forecasting method, smaller *MAPE* indicates better modeling results. These accuracy criteria are defined as [39,40]:

$$RMSE = \sqrt{\frac{1}{n}\sum_{i=1}^{n}(Chl\text{-}a_i - Chl\text{-}a_i')^2} \quad (8)$$

$$MAPE = \frac{1}{n}\sum_{i=1}^{n}\left|\frac{Chl\text{-}a_i - Chl\text{-}a_i'}{Chl\text{-}a_i}\right| \times 100\% \quad (9)$$

where, n refers to the number of samples, and $Chl\text{-}a_i$ and $Chl\text{-}a_i'$ are measured and predicted values of *Chl-a* concentration, respectively.

3. Results and Discussion

3.1. Data Descriptive Statistics

The water quality parameters obtained from field sampling sites showed a high dynamic range and considerable variability (Table 2). The mean Chl-a during the sampling period was 87.35 μg/L, with a maximum of 187.01 μg/L and a minimum of 38.97 μg/L. TSM ranged from 20.98 to 66.60 mg/L (mean = 37.04 mg/L, standard deviation = 8.19 mg/L). OSM and ISM varied from 11.16 to 52.10 mg/L and 0.00 to 28.10 mg/L, with a mean value of 23.54 mg/L and 13.50 mg/L. A total of 93 sample data were randomly divided into two groups: 61 of them were used as training samples for the development of the algorithm, and the remaining 32 samples were used as the validation data set to evaluate the accuracy of the algorithm [41].

Table 2. Statistics of the water quality parameters measured for Chl-a concentration (Chl-a, μg/L), total suspended matter concentrations (TSM, mg/L), organic suspended matter concentrations (OSM, mg/L), and inorganic suspended matter concentrations (ISM, mg/L) from Dianchi Lake. S.D. represents the standard deviation (mg/L), and C.V. represents the coefficient of variation (%).

Sampling Time (YYYY/MM/)	Parameters	Maximum	Minimum	Mean	S.D.	C.V.
Aggregated	Chl-a (μg/L)	187.01	38.97	87.35	24.14	27.64%
(*N* = 93)	TSM (mg/L)	66.60	20.98	37.04	8.19	22.11%
	OSM (mg/L)	52.10	11.16	23.54	8.41	35.73%
	ISM (mg/L)	28.10	0.00	13.50	4.84	35.88%
	OSM/TSM	1.00	0.41	0.63	0.12	19.82%
	ISM/TSM	0.58	0.00	0.37	0.12	33.41%
2009/09	Chl-a (μg/L)	156.69	38.97	93.90	32.91	35.05%
(*N* = 24)	TSM (mg/L)	66.60	24.70	44.40	9.59	21.59%
	OSM (mg/L)	52.10	16.20	35.52	8.35	23.50%
	ISM (mg/L)	22.80	0.00	8.88	4.49	50.55%
	OSM/TSM	1.00	0.41	0.80	0.10	12.98%
	ISM/TSM	0.58	0.00	0.20	0.10	52.94%
2017/04	Chl-a (μg/L)	107.53	61.86	79.69	10.67	13.39%
(*N* = 30)	TSM (mg/L)	50.00	20.98	33.47	6.51	19.46%
	OSM (mg/L)	22.35	11.16	17.85	2.63	14.76%
	ISM (mg/L)	28.10	8.76	15.62	4.67	29.88%
	OSM/TSM	0.69	0.44	0.54	0.06	11.03%
	ISM/TSM	0.56	0.31	0.46	0.06	12.93%
2017/11	Chl-a (μg/L)	187.01	59.67	90.04	25.51	28.33%
(*N* = 39)	TSM (mg/L)	54.37	26.89	36.04	6.07	16.83%
	OSM (mg/L)	36.15	15.50	21.80	4.32	19.82%
	ISM (mg/L)	22.10	7.14	14.24	3.46	24.29%
	OSM/TSM	0.74	0.50	0.61	0.07	11.33%
	ISM/TSM	0.50	0.26	0.39	0.07	17.42%

3.2. Model Development and Validation Based on Simulated-OHS Imagery

3.2.1. Blue-Green Band Ratio Model

This band ratio model can eliminate the atmospheric influence to some extent, and can also reduce the interference of the roughness from the water surface [42]. The blue-green band ratio model is mainly used for Case-I water bodies with phytoplankton as the dominant. The blue-green band ratio model commonly adopted include $R_{rs}(490) > R_{rs}(510)/R_{rs}(560)$, $R_{rs}(490)/R_{rs}(560)$, etc. We referred to the $R_{rs}(490)/R_{rs}(560)$ model in this study, the reflectance ratio factor B2/B7 was used as the independent variable, and the corresponding *Chl-a* concentration was the dependent variable:

$$Chl\text{-}a\_BG = a \times \frac{B2}{B7} + b \tag{10}$$

where, *B2* and *B7* represent the simulated OHS-based remote sensing reflectance at spectral channels of 2nd and 7th band, respectively (the following spectral bands expressions are similar to this), and coefficient $a = -154.84$ and $b = 156.71$ are determined empirically.

3.2.2. Near-Infrared and Red (NIR-Red) Band Ratio Model

The near-infrared and red band ratio model is commonly used in optically complex Case-II water bodies mainly affected by Chl-a concentration, total suspended solids, and colored dissolved organic matter [19]. The generally used near-infrared and red band ratio models are $R_{rs}(700)/R_{rs}(670)$, $R_{rs}(719)/R_{rs}(667)$, $R_{rs}(706)/R_{rs}(682)$, $R_{rs}(708)/R_{rs}(665)$, etc. We referred to the $R_{rs}(708)/R_{rs}(665)$ model in this study:

$$Chl\text{-}a\_NR = a \times \frac{B17}{B14} + b \tag{11}$$

where, coefficient $a = 56.226$ and $b = 0.2191$.

3.2.3. Three-Band Model

The three-band model is based on bio-optical theory and is used for remote sensing retrieval of Chl-a concentration in turbid Case-II water bodies, and its manifestation is $[{R_{rs}}^{-1}(\lambda_1) - {R_{rs}}^{-1}(\lambda_2)]\ R_{rs}(\lambda_3)$, the model is based on three assumptions [43]: (1) the backscattering coefficients of the three bands are approximately equal, that is, $b_b(\lambda_1) \approx b_b(\lambda_2) \approx b_b(\lambda_3)$, where $b_b(\lambda_1)$, $b_b(\lambda_2)$, $b_b(\lambda_3)$ represent the backscattering coefficients at λ_1, λ_2, λ_3, respectively; (2) λ_3 is dominated by the absorption coefficient of pure water, and the absorption coefficients in-water constituents could be ignored, i.e., $a_w(\lambda_3) >> a_{nap}(\lambda_3) + a_{COOM}(\lambda_3) + b_b(\lambda_3)$, where $a_w(\lambda_3)$, $a_{nap}(\lambda_3)$, $a_{COOM}(\lambda_3)$ are the absorption coefficient of pure water, non-pigmented particulate matter and colored dissolved organic matter at λ_3, respectively; (3) the absorption coefficients of non-pigmented particulate matter and colored dissolved organic matter at λ_1 and λ_2 are approximately equal, and λ_1 is located near the absorption peak of Chl-a, namely, $a_{nap}(\lambda_1) \approx a_{nap}(\lambda_2)$, $a_{COOM}(\lambda_1) \approx a_{COOM}(\lambda_2)$ and $a_{ph}(\lambda_1) >> a_{ph}(\lambda_2)$ where $a_{ph}(\lambda_1)$ and $a_{ph}(\lambda_2)$ are the absorption coefficient of phytoplankton pigment particles at λ_1 and λ_2, respectively. Regularly used band combination forms of three-band model are $[{R_{rs}}^{-1}(690) - {R_{rs}}^{-1}(693)]R_{rs}(800)$, $[{R_{rs}}^{-1}(666) - {R_{rs}}^{-1}(688)]R_{rs}(725)$, $[{R_{rs}}^{-1}(671) - {R_{rs}}^{-1}(710)]R_{rs}(740)$, and $[{R_{rs}}^{-1}(753) - {R_{rs}}^{-1}(665)]R_{rs}(708)$, etc. By analyzing the optical properties of the Dianchi Lake waters, we found that the above conditions were satisfied when $\lambda_1 = 680$ nm, $\lambda_2 = 710$ nm, and $\lambda_3 = 745$ nm, and the three-band model used in this study is:

$$Chl\text{-}a\_TB = a \times [1/B15 - 1/B17] \times B19 + b \tag{12}$$

where, $a = 137.35$ and $b = 59.741$.

3.2.4. Four-Band Model

Due to the optically complex properties of inland eutrophic lakes, the assumptions in the three-band model cannot be established simultaneously. For this reason, a new near-infrared band was introduced in the four-band model to reduce the impact of the absorption of pure water and non-pigmented particles on estimation of the Chl-a concentration [44]. We referred to the method described by Le et al. [44] for the four-band model, namely, $[R_{rs}{}^{-1}(662) - R_{rs}{}^{-1}(693)]$ $[R_{rs}{}^{-1}(740) - R_{rs}{}^{-1}(705)]$:

$$Chl\text{-}a\_FB = a \times \frac{1/B13 - 1/B15}{1/B19 - 1/B16} + b \quad (13)$$

where, $a = -0.0002$ and $b = 89.498$.

3.2.5. Fluorescence Line Height (FLH) Model

The fluorescence line height model was first proposed by Neville & Gower [45] to be applied to the estimation of Chl-a concentration in various types of water. This method is based on the relationship between the peak distance from the baseline and the Chl-a concentration. The fluorescence line height model is as follows:

$$FLH = B15 - \left[B17 + (B14 - B17) \times \frac{\lambda_{B17} - \lambda_{B15}}{\lambda_{B17} - \lambda_{B14}}\right] \quad (14)$$

$$Chl\text{-}a\_FLH = a \times FLH + b \quad (15)$$

where, $a = -11510$ and $b = 75.573$; λ_{B14}, λ_{B15}, and λ_{B17} are central wavelength of 14th, 15th, and 17th band of OHS imagery, respectively.

3.2.6. Model Validation Based on Simulated-OHS Imagery

Model validation was used to assess the effect of the Chl-a concentration estimation model and the existing uncertainty and can be used to evaluate whether the retrieval algorithm has practical application value. In this study, the root mean square error (RMSE) and the mean absolute percentage error (MAPE) were used to assess the accuracy of the Chl-a concentration estimation model via Formulas (8) and (9), and to analyze the accuracy difference and uncertainty among different algorithms (Figure 3 and Table 3).

Table 3. Estimation model of Chl-a concentration based on simulated OHS imagery. R^2, RMSE, and MAPE represent the determination coefficient, root-mean-square error, and mean absolute percentage error, respectively.

Model Name	Variable (x)	For Form	R^2	RMSE (μg/L)	MAPE
Blue-Green Band Ratio	B2/B7	Chl-a_BG = $-154.84x + 156.71$	0.144	22.97	24.78%
NIR-Red Band Ratio	B17/B14	Chl-a_NR = $56.226x + 0.2191$	0.729	17.78	17.16%
Three-band	(1/B15–1/B17)B19	Chl-a_TB = $137.35x + 59.741$	0.809	15.55	16.31%
Four-band	(1/B13–1/B15) (1/B19–1/B16)	Chl-a_FB = $-0.0002x + 89.498$	0.001	24.44	28.17%
FLH	FLH	Chl-a_FLH = $-11510x + 75.573$	0.636	22.40	21.59%

As shown in Figure 3 and Table 3, the effect of the four-band model was the worst ($RMSE$ = 24.44 μg/L, $MAPE$ = 28.17%); the three-band model had the highest accuracy ($RMSE$ = 15.55 μg/L, $MAPE$ = 16.31%) with the error within the acceptable range, which was suitable for the remote estimation of the Chl-a concentration in Dianchi Lake. The results of the estimation model were validated based on the simulated OHS imagery.

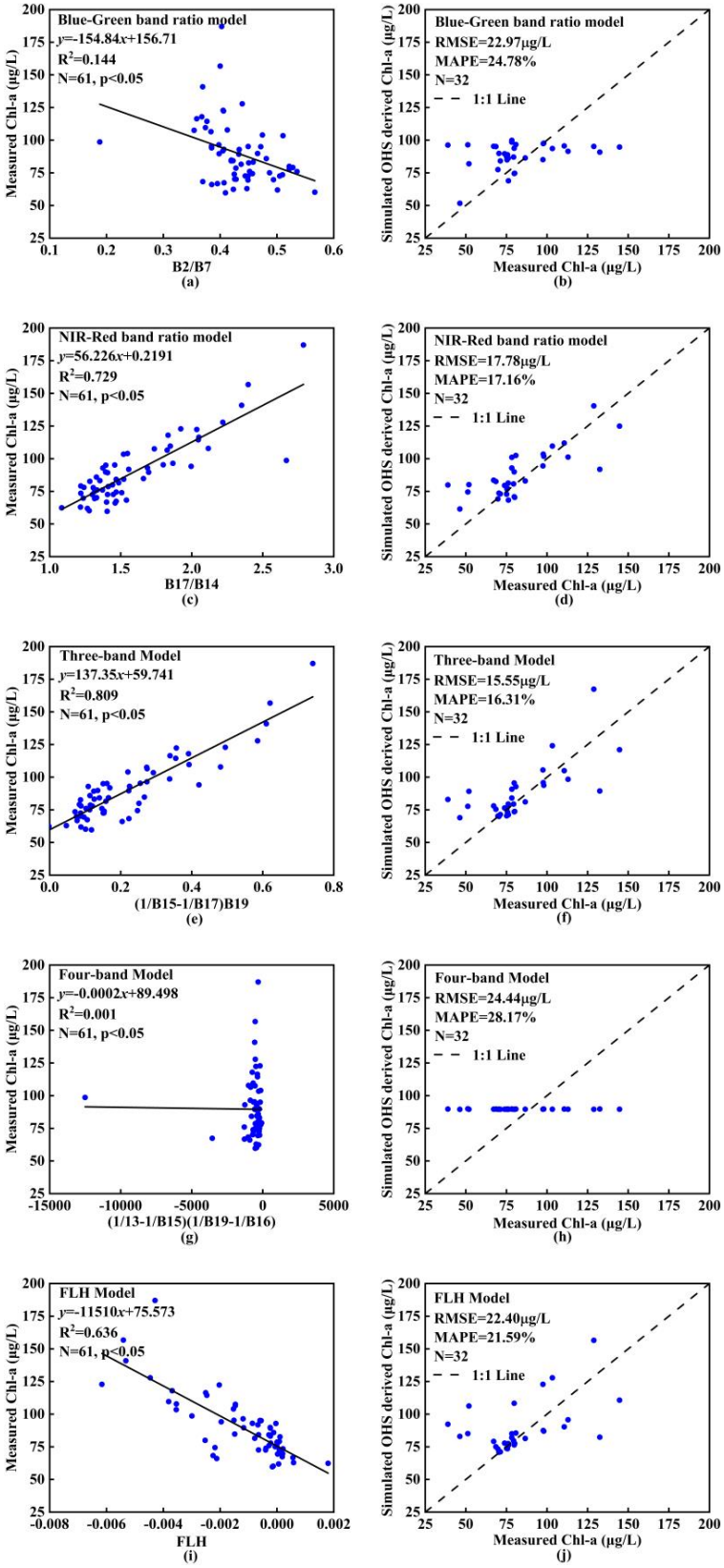

Figure 3. Scatter-plots of Chl-a model development (**a**–**i**) between measured in situ Chl-a data and simulated OHS-based derived R_{rs}, and Chl-a model validation (**b**–**j**) between measured and simulated OHS-based derived Chl-a through Equations (10)–(15). Chl-a is chlorophyll-a concentration and OHS is OHS imagery.

3.3. Validation and Spatial Patterns of Chl-a from OHS Imagery

3.3.1. Validation of Derived Chl-a for OHS Imagery

To further assess the effectiveness of the three-band algorithm for the OHS image, the measured Chl-a concentration data synchronized with OHS imagery from 10 observation stations evenly distributed in Dianchi Lake on 2 April 2019 (OHS imaging date) were used for model evaluation. In order to determine the influence of atmospheric correction on Chl-a concentration inversion, we used satellite–ground synchronization data to validate the Chl-a concentration retrieval results obtained by applying different atmospheric correction algorithms such as the FLAASH model, 6S model, QUAC model, and dark pixel method (Figure 4). Among them, the FLAASH model had the best validation effect (m *MAPE* = 8.26%) and could be applied to the atmospheric correction of the OHS imagery of Dianchi Lake, while the Chl-a concentration obtained by the 6S atmospheric correction model was significantly higher than the in situ Chl-a concentration (*RMSE* = 31.49 μg/L, *MAPE* = 56.86%), and was not suitable for the OHS imagery of Dianchi Lake. The Chl-a concentration estimated based on the three-band model had a significant correlation with the measured Chl-a concentration (R^2 = 0.858, $p < 0.05$) with RMSE of 5.71 μg/L and MAPE of 8.26% of the relative difference (Figure 4). Comparisons between the in situ Chl-a measured and the Chl-a estimated using the proposed three-band model in this study showed that these values were acceptable. These results indicate that the three-band model could be used with satisfactory performance to retrieve Chl-a concentration in this inland water body.

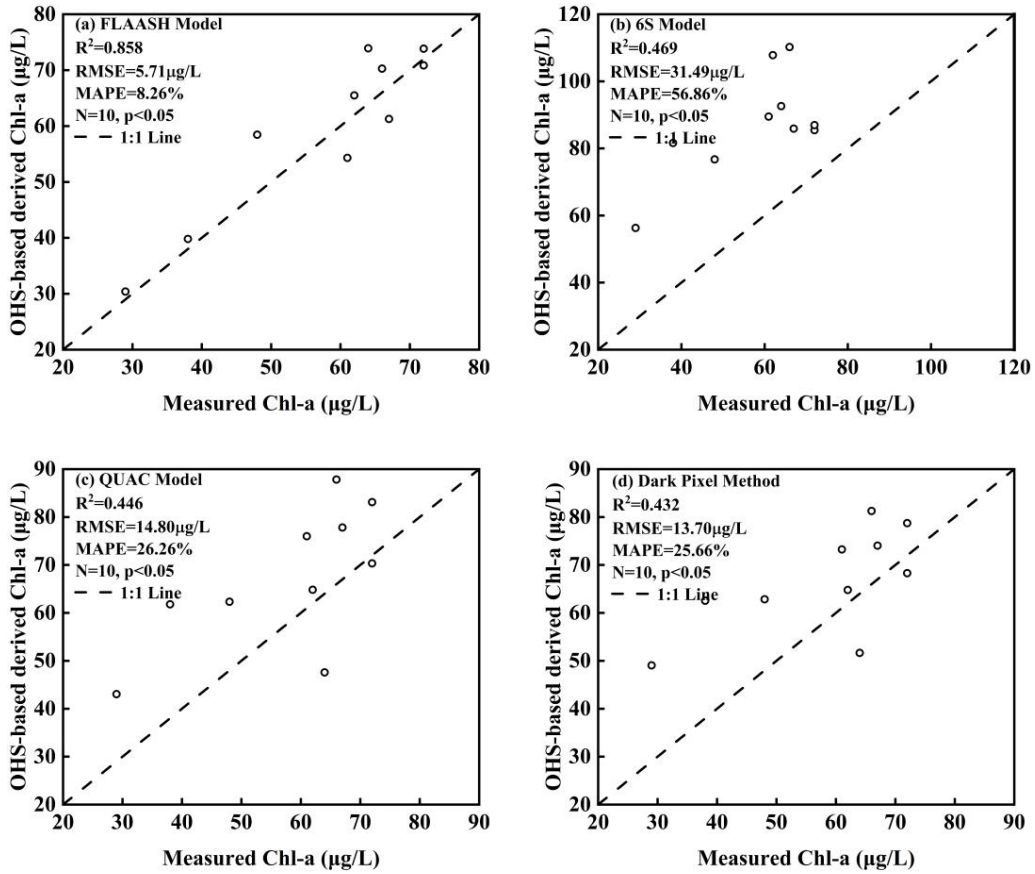

Figure 4. Comparison of OHS-derived and measured Chl-a for OHS imagery. (**a**–**d**) respectively represent the validation of Chl-a concentration inversion results after using different atmospheric correction algorithms such as the FLAASH model, 6S model, QUAC model, and dark pixel method.

3.3.2. Spatial Patterns of Chl-a in Dianchi Lake

The three-band model was applied to the OHS imagery to obtain the spatial distribution pattern of Chl-a concentration in Dianchi Lake (Figure 5a), which revealed that the concentration of Chl-a in Dianchi Lake showed an increasing trend from the center of the lake to the coast of the lake. To quantitatively reveal the spatial distribution characteristics of Chl-a concentration in Dianchi Lake, three cross-section lines were randomly selected to analyze the variation of Chl-a concentration with the distance from the lakeshore. Figure 5b intuitively describes the overall decreasing trend of Chl-a concentration as the distance from the lake shore increases. The center of the lake had the lowest concentration of Chl-a, being 20~40 μg/L; the Chl-a concentration along the lake was the highest, reaching 100~180 μg/L; and the mean Chl-a concentration of the whole Dianchi Lake on 2 April 2019, was estimated to be 66.43 ± 12.98 μg/L.

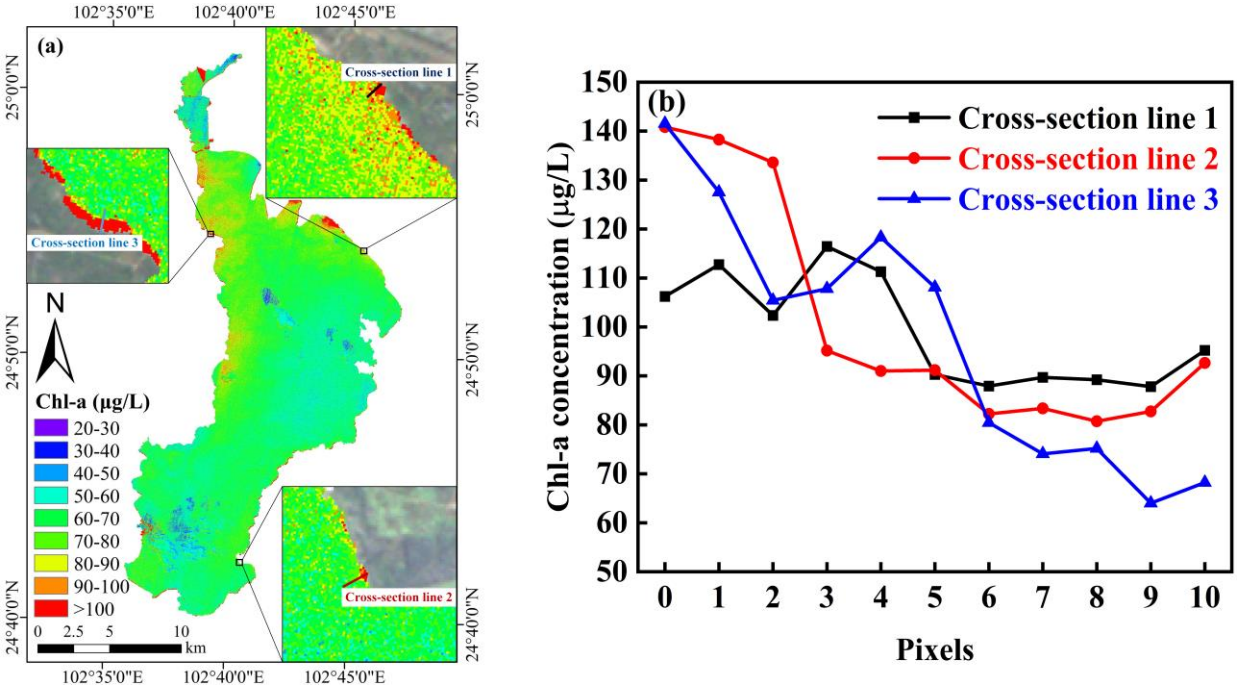

Figure 5. Spatial patterns of derived Chl-a concentration in Dianchi Lake on 2 April 2019. (**a**) describes the spatial distribution of Chl-a concentration in Dianchi Lake. (**b**) is the three cross-sections randomly selected in (**a**) to quantitatively express the variation of Chl-a concentration with the distance from the lakeshore.

3.4. Uncertainty Analysis of OHS Imagery

3.4.1. Signal-to-Noise Ratio of OHS Imagery

In order to compare the SNR of the OHS image with other multispectral and hyperspectral images, Landsat-8 OLI (Operational Land Imager) (spatial resolution of 30 m), Sentinel-2 MSI (Multispectral Instrument, spatial resolution of 10 m, 20 m and 60 m), EO-1 Hyperion (Earth Observing-1, spatial resolution of 30 m), and HJ-1 HSI (Hyperspectral Imager, spatial resolution of 100 m) were selected to perform comparable analysis with OHS imagery. A comparatively large area with relatively stable bio-optical properties in Dianchi Lake was selected as the SNR study area (Figure 6a). Simultaneously, the OHS imagery was resampled to 30 m and 100 m to explore the effect of spatial resolution on the SNR of the OHS imagery. The SNR of the Landsat-8 OLI imagery was significantly higher than that of the OHS imagery, Hyperion imagery, HSI imagery, and Sentinel-2 imagery, but it gradually decreased with wavelength increase. The SNR of multispectral images was generally higher than that of hyperspectral images. The SNR of the HSI image in all bands was relatively low, indicating that as the spectral resolution advances, the noise decreases accordingly. The SNR of the Hyperion imagery gradually declined with the increase of

the wavelength, which was similar to that of the OHS imagery. Although the SNR of OHS imagery after resampling has improved, the change was not obvious, reflecting that the spatial resolution had no significant effect on the OHS imagery (Figure 6b,c, Table 4). This result is different from the change of multi-spectral image SNR with spatial resolution [46].

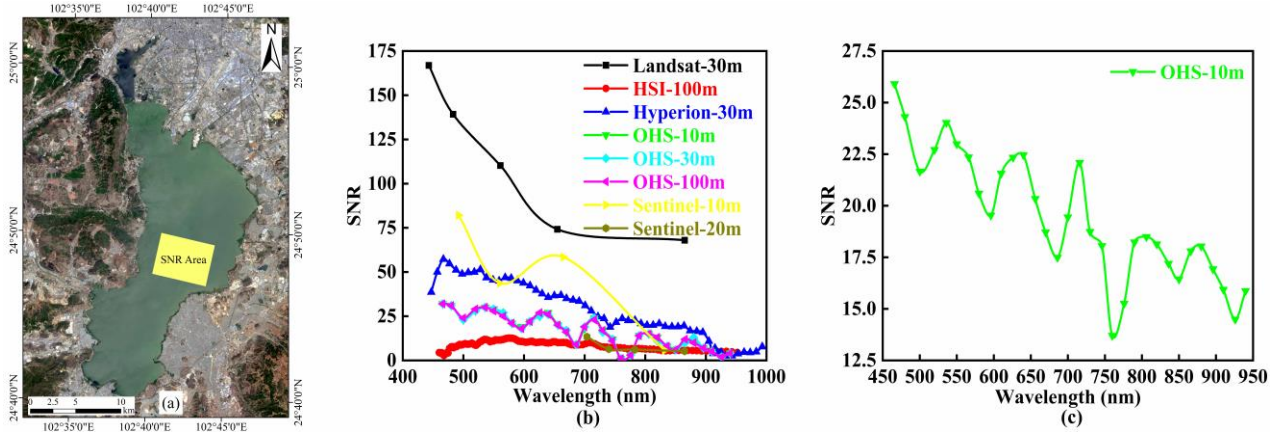

Figure 6. The signal-to-noise ratio comparison between OHS image, Landsat-8 image, and HSI image. (**a**) indicates the selected SNR calculation area. (**b**) designates the SNR of different images (the black line is the SNR of the Landsat-8 image, the red line is the SNR of the HSI image, the blue line is the SNR of the Hyperion image, the green line is the SNR of the OHS image (spatial resolution of 10 m), the cyan line is the SNR of the OHS image (spatial resolution of 30 m), the pink line is the SNR of the OHS image (spatial resolution of 100 m), the yellow line is the SNR of the Sentinel-2 image (spatial resolution of 10 m), the brown line is the SNR of the Sentinel-2 image (spatial resolution of 20 m)). (**c**) denotes the stretched version of the SNR of the OHS imagery (spatial resolution of 10 m) in (**b**).

Table 4. Comparison of the SNR of OHS image, Landsat-8 OLI image, HJ-1 HSI image, EO-1 Hyperion image, and Sentinel-2 MSI image for typical bands.

Images	Coastal Aerosol (435–451 nm)	Blue (452–512 nm)	Green (532–600 nm)	Red (635–673 nm)	NIR (845–892 nm)
OHS-10 m	25.91	24.31	22.99	20.34	17.80
OHS-30 m	26.03	24.25	22.88	20.33	17.77
OHS-100 m	26.62	24.71	22.70	20.32	18.07
Landsat-8 OLI-30 m	166.87	139.23	110.25	74.18	67.97
HJ-1 HSI-100 m	4.41	7.71	11.53	10.07	5.61
EO-1 Hyperion-30 m	38.63	51.14	44.97	36.63	19.54
Sentinel-2 MSI-10 m	——	82.13	43.66	58.40	5.75
Sentinel-2 MSI-20 m	——	——	——	——	5.18
Sentinel-2 MSI-60 m	127.60	——	——	——	——

The SNR of the OHS image generally decreased with increasing wavelength, and there was an obvious minimum near 760 nm (Figure 6). As a result of the weak water signal in watercolor and the low SNR of high spatial resolution sensors, it was difficult to distinguish the subtle differences among signals, limiting its application in watercolor remote sensing to some extent and reducing the accuracy of Chl-a concentration estimation.

3.4.2. Limitation

The three-band model based on simulated OHS imagery proposed in this study has successfully retrieved the Chl-a concentration in eutrophic plateau lakes but still has the following limitations: (1) Limitations of the application area. Compared with the existing Chl-a concentration retrieval algorithms [19,47–52] (Tables A2 and A3, Figures A1–A4), the three-band model developed in this study is most suitable for remote sensing retrieval of Chl-a concentration in eutrophic plateau lakes. However, due to the optically complex properties of the water body, whether the three-band model proposed in this study is

applicable to other optical water types such as Dongting Lake and Poyang Lake is still unknown. In addition, the three-band model developed in this study is an empirical algorithm, which appears to rely on measured data. Therefore, for different in situ data sets, the model coefficients may vary, and the model needs to be re-calibrated. (2) Limitations of OHS imagery. This study only discusses the capability of OHS imagery to monitor the water quality in eutrophic plateau lakes; further research needs to be undertaken on whether OHS imagery could be applied to other types of water bodies or other application fields such as vegetation remote sensing.

4. Conclusions

A new and customized Chl-a concentration retrieval algorithm based on measured spectral data and OHS imagery is proposed in this study. The model improved Chl-a estimation accuracy using the OHS imagery in extremely eutrophic plateau water bodies compared to the existing models proposed for clear open sea and turbid coastal waters. This was then used to document the temporal and spatial patterns of Chl-a distributions in Dianchi Lake, leading to several key findings.

First, the three-band model based on OHS imagery is most suitable for estimating the concentration of Chl-a in Dianchi Lake, with RMSE and MAPE of 15.55 μg/L and 16.31%, respectively.

Second, the patterns of Chl-a retrieval from OHS imagery exhibit a significant spatial heterogeneity in Dianchi Lake, which is significantly higher in the surrounding region than the central waters.

Third, the FLAASH model is appropriate for estimating the concentration of Chl-a in Dianchi Lake, while the 6S model, QUAC model, and dark pixel method are not suitable for eutrophic Dianchi waters.

Moreover, the SNR of the OHS image (mean value of 19.43) is similar to that of the Hyperion image (mean value of 27.87) but nearly 2.5 times SNR of the HSI image (mean value of 8.47), and the variations in spatial resolution do not show a significant effect on the SNR of the OHS image. The findings indicated that the performance of SNR is much improved from HSI to OHS imagery; however, further improvement is still needed since there is still a gap compared with advanced hyperspectral imageries, such as Hyperion, etc.

Lastly, OHS imagery can be applied to remote sensing retrieval of Chl-a concentration in eutrophic plateau lakes.

Author Contributions: R.Z. contributed to the research method, carried out data analysis, and wrote the manuscript. Z.Z. had the original idea for the study and was responsible for the recruitment and follow-up of study participants, manuscript review, and funding. G.L., C.D. (Chenggong Du) and C.D. (Chao Du) contributed to the research method. C.D. (Chao Du), S.L. and Y.X. performed the processing of data. J.X., M.M., S.B. and J.L. acquired remote sensing data. All authors have read and agreed to the published version of the manuscript.

Funding: This research was funded by the National Natural Science Foundation of China (No. 41701412; 41907331), Natural Science Foundation of Jiangxi Province (No. 20171BAB213024), Natural Science Foundation of Jiangsu Province (BK20191058), and Natural Science Research Project of Jiangsu Higher Education Institution (19KJB170001).

Institutional Review Board Statement: Not applicable.

Informed Consent Statement: Not applicable.

Data Availability Statement: The data presented in this study are available upon request from the corresponding author.

Acknowledgments: This research received financial support from the National Natural Science Foundation of China (No. 41701412; 41907331), the Natural Science Foundation of Jiangxi Province (No. 20171BAB213024), Natural Science Foundation of Jiangsu Province (BK20191058), and Natural Science Research Project of Jiangsu Higher Education Institution (19KJB170001). The field measurement data set of Dianchi Lake used in this research comes from the Water Environment

Remote Sensing Research Group of the Key Laboratory of Virtual Geography Environment of the Ministry of Education of Nanjing Normal University. We sincerely thank Yunmei Li for her help and the hard work of the experimental staff. We would like to appreciate Zhuhai Orbita Aerospace Technology Co., Ltd. and Dianchi Administration Bureau for providing remote sensing data and in situ chlorophyll-a concentration data respectively. We are deeply grateful to the three anonymous reviewers and academic editors for their constructive comments and suggestions to improve the quality of this work.

Conflicts of Interest: The authors declare no conflict of interest.

Appendix A

Table A1. OHS image bands setting and radiometric calibration coefficient. Wavelength represents the central wavelength of each band, FWHM (Full-Width Half-Maximum) is the wave width of each band, Radiance Gains and Radiance Offsets are the radiometric calibration gain coefficient and offset coefficient respectively, TDIStage is the integration series. The parts in bold are the bands used in this study.

Bands	Wavelength (nm)	FWHM (nm)	Radiance Gains ($W \cdot m^{-2} \cdot sr^{-1} \cdot \mu m^{-1}$)	Radiance Offsets ($W \cdot m^{-2} \cdot sr^{-1} \cdot \mu m^{-1}$)	TDIStage
B1	466	5.0	0.31711	0.00000	6
B2	**480**	**5.0**	**0.33824**	**0.00000**	**6**
B3	500	5.0	0.42547	0.00000	6
B4	520	6.0	0.45222	0.00000	6
B5	536	6.0	0.45314	0.00000	6
B6	550	7.0	0.47178	0.00000	6
B7	**566**	**7.0**	**0.43948**	**0.00000**	**6**
B8	580	8.0	0.42103	0.00000	6
B9	596	8.0	0.46463	0.00000	5
B10	610	7.0	0.41791	0.00000	5
B11	626	8.0	0.37667	0.00000	5
B12	640	8.0	0.36352	0.00000	5
B13	**656**	**8.0**	**0.39356**	**0.00000**	**4**
B14	**670**	**9.0**	**0.38094**	**0.00000**	**4**
B15	**686**	**10.0**	**0.31421**	**0.00000**	**4**
B16	**700**	**10.0**	**0.42416**	**0.00000**	**3**
B17	**716**	**10.0**	**0.36147**	**0.00000**	**3**
B18	730	10.0	0.38121	0.00000	3
B19	**746**	**10.0**	**0.35642**	**0.00000**	**3**
B20	760	10.0	0.28216	0.00000	3
B21	776	9.0	0.36163	0.00000	3
B22	790	12.0	0.34793	0.00000	3
B23	806	11.0	0.36328	0.00000	3
B24	820	12.0	0.35926	0.00000	3
B25	836	9.0	0.38408	0.00000	3
B26	850	11.0	0.38707	0.00000	3
B27	866	11.0	0.38515	0.00000	3
B28	880	12.0	0.32043	0.00000	4
B29	896	11.0	0.28990	0.00000	5
B30	910	11.0	0.30713	0.00000	5
B31	926	14.0	0.34246	0.00000	6
B32	940	13.0	0.22125	0.00000	8

Table A2. Comparison between this study and existing Chl-a concentration inversion algorithms and commonly used ocean color satellite images. GOCI represents Geostationary Ocean Color Imager; OLCI describes Ocean and Land Colour Instrument; SCI stands for Synthetic Chlorophyll Index algorithm.

Model	Model Form	Study Region	Image Applied	RMSE (μg/L)	MAPE
Gurlin et al. [19]	$R_{rs}(748)/R_{rs}(667)$	Fremont Lakes	MODIS	6.10	27.6%
	$R_{rs}(709)/R_{rs}(665)$	Fremont Lakes	MERIS	3.60	11.6%
	$(R_{rs}^{-1}(665)\text{-}R_{rs}^{-1}(709))R_{rs}(754)$	Fremont Lakes	MERIS	3.30	18.0%
Bi et al. [47]	FLH	Erhai Lake	OLCI	1.92	13.5%
	$(R_{rs}^{-1}(665)\text{-}R_{rs}^{-1}(709))R_{rs}(754)$	Erhai Lake	OLCI	1.61	12.4%
Yang et al. [48]	$(R_{rs}^{-1}(665)\text{-}R_{rs}^{-1}(709))(R_{rs}^{-1}(754)\text{-}R_{rs}^{-1}(709))$	Kasumigaura Lake	MERIS	8.68	12.3%
Guo et al. [49]	$(R_{rs}^{-1}(680)\text{-}R_{rs}^{-1}(660))R_{rs}(745)$	Taihu Lake	GOCI	16.31	32.5%
	$(R_{rs}^{-1}(681)\text{-}R_{rs}^{-1}(709))R_{rs}(754)$	Taihu Lake	GOCI	15.17	26.5%
Härmä et al. [50]	$(R_{rs}(531)\text{-}R_{rs}(748))(R_{rs}(551)\text{-}R_{rs}(748))$	Finland Lake	MODIS	11.60	77.0%
Du et al. [51]	$(R_{rs}^{-1}(691)\text{-}R_{rs}^{-1}(722))R_{rs}(854)$	Taihu Lake	Hyperion	13.93	23.7%
Lyu et al. [52]	SCI	Taihu Lake	MERIS	4.89	38.1%
	$(R_{rs}^{-1}(665)\text{-}R_{rs}^{-1}(709))R_{rs}(779)$	Taihu Lake	MERIS	15.67	24.5%
	$(R_{rs}^{-1}(665)\text{-}R_{rs}^{-1}(709))(R_{rs}^{-1}(865)\text{-}R_{rs}^{-1}(709))$	Taihu Lake	MERIS	7.88	31.3%
This study	$(R_{rs}^{-1}(686)\text{-}R_{rs}^{-1}(716))R_{rs}(746)$	Dianchi Lake	OHS	15.55	16.31%

Table A3. Comparison of Chl-a concentration estimation results of this study and existing algorithms applied to Dianchi Lake. Bi is the band of the OHS image corresponding to the wavelength in the citation. SCI stands for Synthetic Chlorophyll Index algorithm.

Model	Variable (x)	Model Form	R^2	RMSE (μg/L)	MAPE
Gurlin et al. [19]	B19/B14	Chl-a = $110.03x - 0.4494$	0.691	21.10	22.41%
	B16/B14	Chl-a = $54.529x - 7.5799$	0.452	20.79	23.01%
	(1/B14-1/B16)B20	Chla = $142.93x + 40.651$	0.712	21.64	23.35%
Bi et al. [47]	FLH	Chl-a = $-11510x + 75.573$	0.636	22.40	21.59%
	(1/B14-1/B16)B20	Chl-a = $142.93x + 40.651$	0.712	20.68	23.29%
Yang et al. [48]	(1/B14-1/B16)(1/B20-1/B16)	Chl-a = $8*10^{-6}x + 89.593$	0.000	24.43	28.15%
Guo et al. [49]	(1/B15-1/B13)B19	Chl-a = $273.31x + 52.424$	0.515	21.32	21.69%
	(1/B15-1/B16)B20	Chl-a = $178.45x + 42.631$	0.738	21.23	21.87%
Härmä et al. [50]	(B5-B19)(B6-B19)	Chl-a = $-17937x + 94.359$	0.017	24.62	28.46%
Du et al. [51]	(1/B15-1/B17)B26	Chl-a = $190.48x + 65.261$	0.602	20.26	20.16%
Lyu et al. [52]	SCI	Chl-a = $4841.8x + 57.761$	0.120	21.64	24.71%
	(1/B14-1/B16)B21	Chl-a = $143.67x + 39.666$	0.718	20.55	22.81%
	(1/B14-1/B16)(1/B27-1/B16)	Chl-a = $-0.0002x + 90.107$	0.003	24.45	28.00%
This study	(1/B15-1/B17)B19	Chl-a = $137.35x + 59.741$	0.809	15.55	16.31%

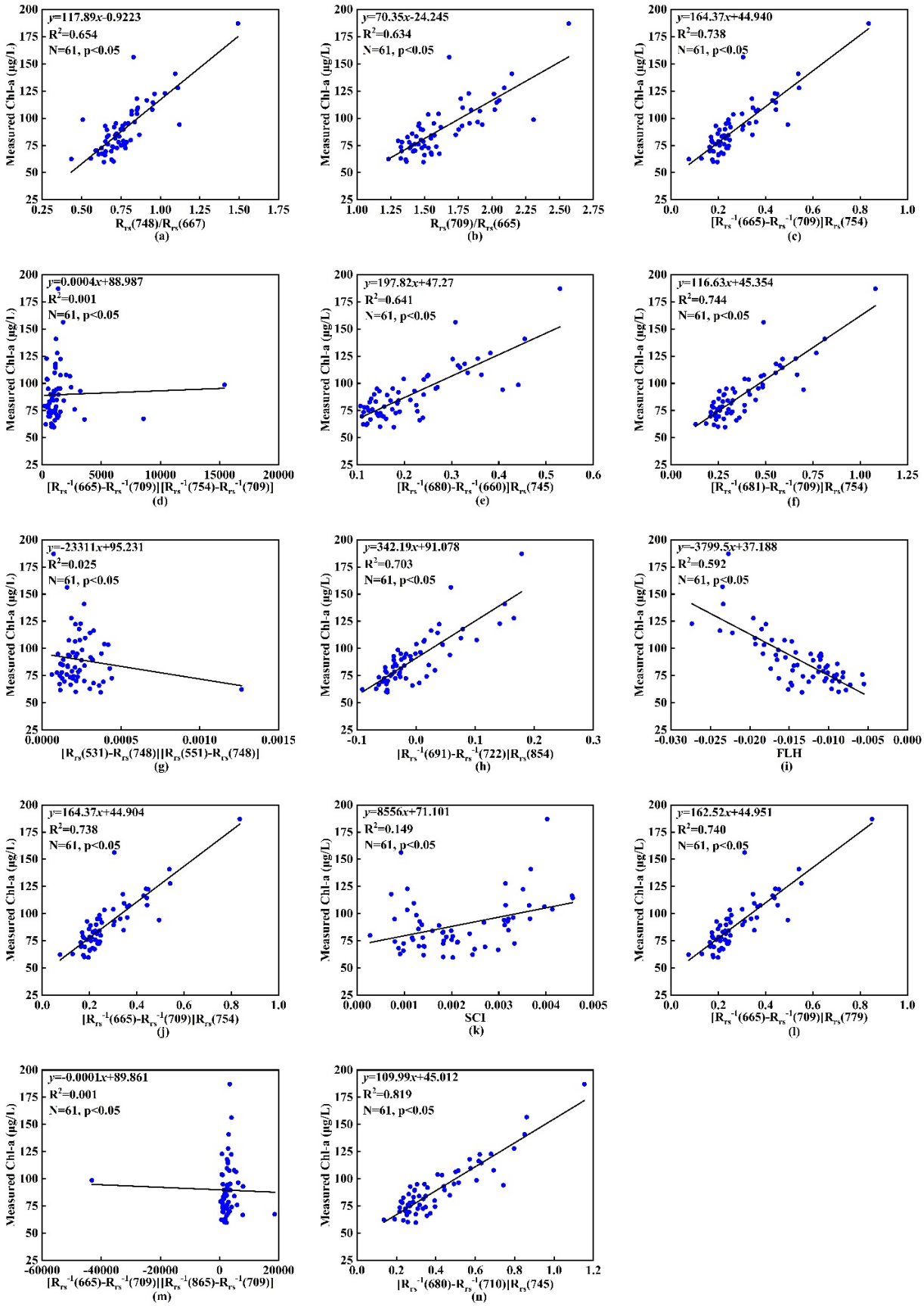

Figure A1. Comparison of existing Chl-a concentration retrieval algorithms based on measured data. (**a**–**n**) are the models reconstructed by applying the algorithms in Table A2 to Dianchi Lake through calibration parameters.

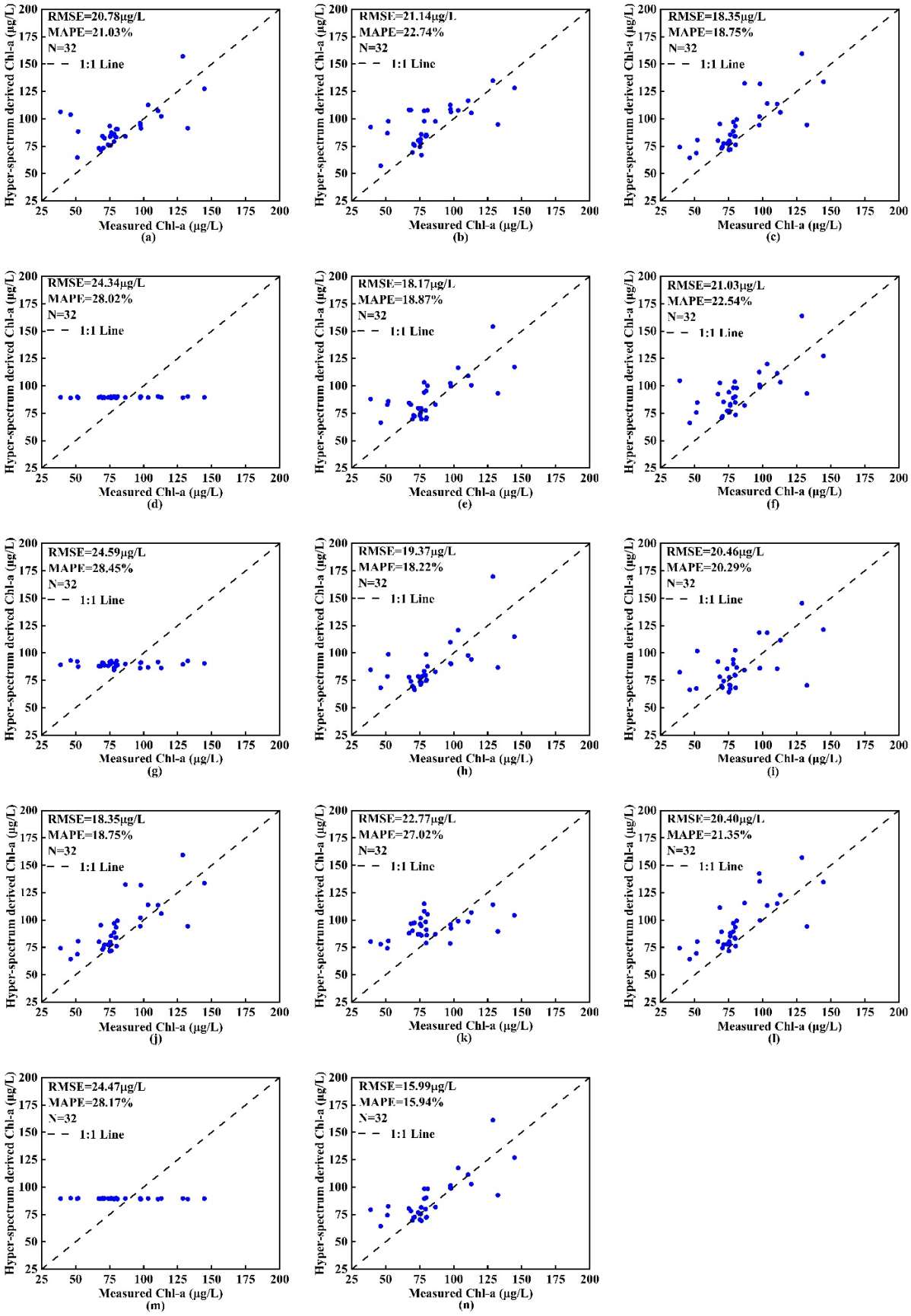

Figure A2. Comparison of the validation results of existing Chl-a concentration retrieval algorithms based on measured data. (**a**–**n**) are the validation of the reconstruction models in Figure A1 in turn.

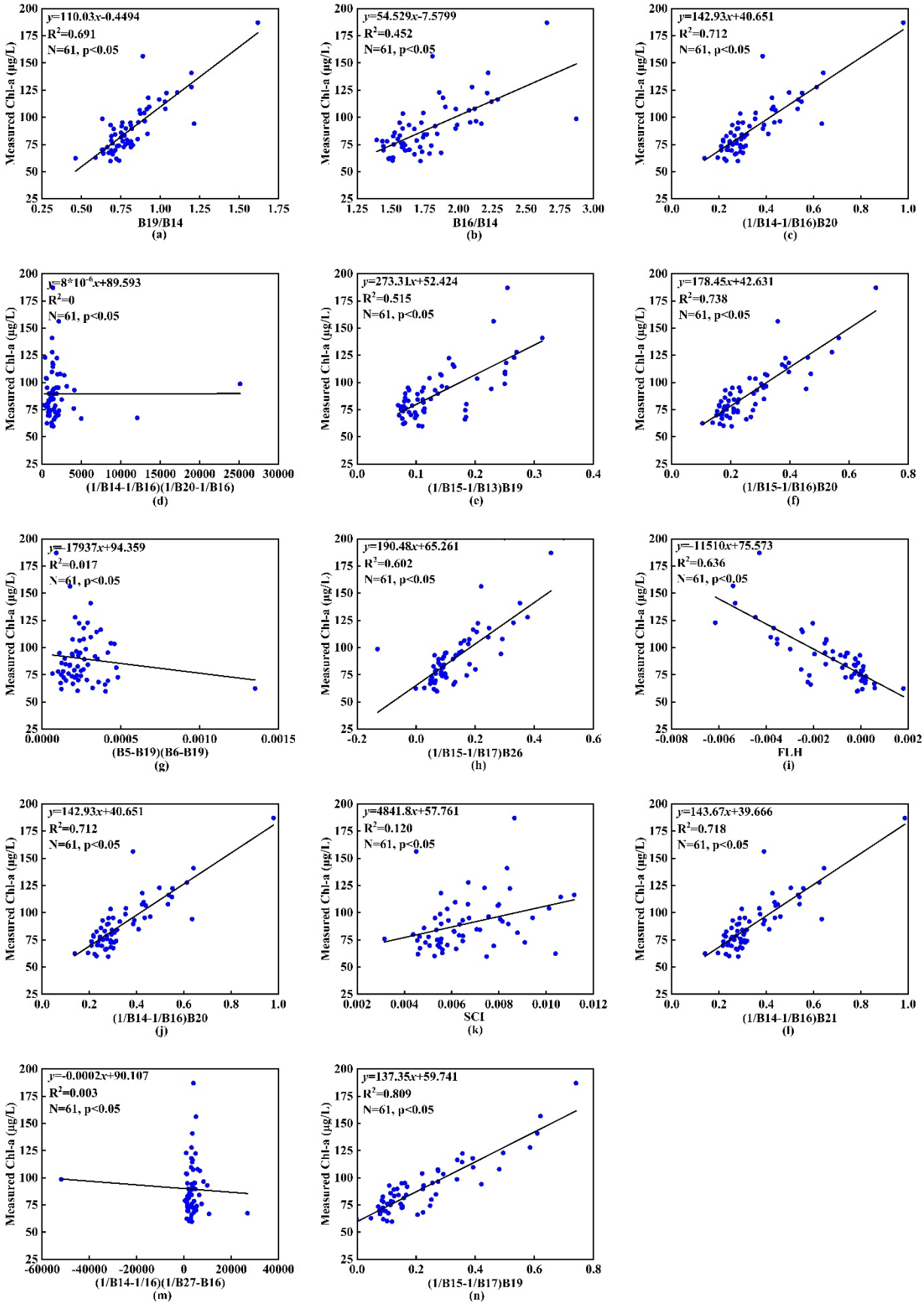

Figure A3. Comparison of existing Chl-a concentration retrieval algorithms based on OHS imagery. (**a**–**n**) are the models reconstructed by applying the algorithms in Table A3 to Dianchi Lake through calibration parameters.

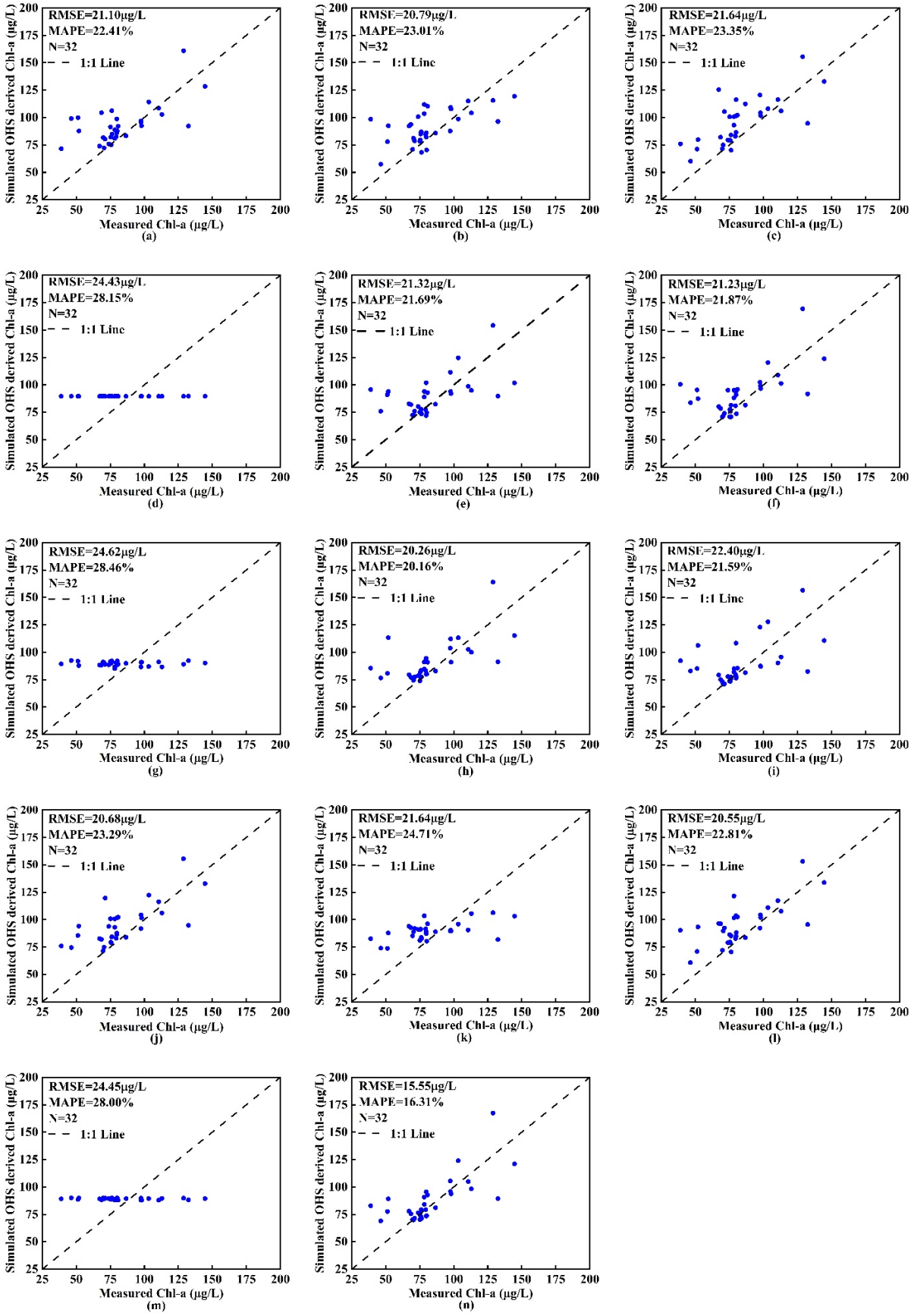

Figure A4. Comparison of the results of existing Chl-a concentration retrieval algorithms based on OHS imagery. (**a**–**n**) are the validation of the reconstruction models in Figure A3 in turn.

References

1. Ma, R.H.; Tang, J.W.; Duan, H.T.; Pan, D.L. Progress in lake water color remote sensing. *J. Lake Sci.* **2009**, *21*, 143–158. (In Chinese)
2. Beck, R.; Zhan, S.G.; Liu, H.X.; Tong, S.S.; Yang, B.; Xu, M.; Ye, Z.X.; Huang, Y.; Shu, S.; Wu, Q.S.; et al. Comparison of satellite reflectance algorithms for estimating chlorophyll-a in a temperate reservoir using coincident hyperspectral aircraft imagery and dense coincident surface observations. *Remote Sens. Environ.* **2016**, *178*, 15–30. [CrossRef]
3. Tilstone, G.; Mallor-Hoya, S.; Gohin, F.; Couto, A.B.; Sá, C.; Goela, P.; Cristina, S.; Airs, R.; Icely, J.; Zühlke, M. Which ocean colour algorithm for MERIS in North West European waters? *Remote Sens. Environ.* **2017**, *189*, 132–151. [CrossRef]
4. Falkowski, P.G.; Scholes, R.J.; Boyle, E.; Canadell, J.; Canfield, D.; Elser, J. The global carbon cycle: A test of our knowledge of Earth as a system. *Science* **2000**, *290*, 291–296. [CrossRef] [PubMed]
5. Honeywill, C.; Paterson, D.M.; Hegerthey, S.E. Determination of microphy-tobenthic biomass using pulse-amplitude modulated minimum fluorescence. *Eur. J. Phycol.* **2002**, *37*, 485–492. [CrossRef]
6. Birk, S.; Bonne, W.; Borja, A.; Brucet, S.; Courrat, A.; Poikane, S.; Solimini, A.; van de Bund, W.; Zampoukas, N.; Hering, D. Three hundred ways to assess Europe's surface waters: An almost complete overview of biological methods to implement the Water Framework Directive. *Ecol. Indic.* **2012**, *18*, 31–41. [CrossRef]
7. Chang, N.B.; Imen, S.; Vannah, B. Remote sensing for monitoring surface water quality status and ecosystem state in relation to the nutrient cycle: A 40-year perspective. *Crit. Rev. Environ. Sci. Technol.* **2015**, *45*, 101–166. [CrossRef]
8. Simisa, S.G.H.; Ruiz-Verdúb, A.; Domínguez-Gómezb, J.A.; Peña-Martinezb, R.; Petersc, S.W.M.; Gonsa, H.J. Influence of phytoplankton pigment composition on remote sensing of cyanobacterial biomass. *Remote Sens. Environ.* **2007**, *106*, 414–427. [CrossRef]
9. Zhang, C.Y.; Hu, C.M.; Shang, S.L. Bridging between SeaWiFS and MODIS for continuity of chlorophyll-a concentration assessments off Southeastern China. *Remote Sens. Environ.* **2006**, *102*, 250–263. [CrossRef]
10. Kudela, R.M.; Palacios, S.L.; Austerberry, D.C.; Accorsi, E.K.; Guild, L.S.; Torres-Perez, J. Application of hyperspectral remote sensing to cyanobacterial blooms in inland waters. *Remote Sens. Environ.* **2015**, *167*, 196–205. [CrossRef]
11. Li, Y.M.; Wang, Q.; Wu, Q.C.; Zhao, S.H.; Xu, X.; Wang, Y.F.; Hang, C.C. Estimation of Chlorophyll a Concentration Using NIR/Red Bands of MERIS and Classification Procedure in Inland Turbid Water. *Trans. Geosci. Remote Sens.* **2011**, *50*, 988–997. [CrossRef]
12. Zeng, Q.; Zhang, H.D.; Chen, X.L.; Tian, L.Q.; Li, W.K.; Wang, G.L. Evaluation on the atmospheric correction methods for water color remote sensing by using MERIS image: A case study on chlorophyll-a concentration of Lake Poyang. *J. Lake Sci.* **2016**, *28*, 1306–1315. (In Chinese) [CrossRef]
13. Duan, H.T.; Zhang, Y.Z.; Zhang, B.; Song, S.K.; Wang, Z.M. Assessment of chlorophyll-a concentration and trophic state for Lake Chagan using Landsat TM and field spectral data. *Environ. Monit. Assess.* **2007**, *129*, 295–308. [CrossRef] [PubMed]
14. Fang, X.; Duan, H.T.; Cao, Z.G.; Shen, M.; Ge, X.S. Remote monitoring of cyanobacterial blooms using multi-source satellite data: A case of Yuqiao Reservoir, Tianjin. *J. Lake Sci.* **2018**, *30*, 967–978. (In Chinese) [CrossRef]
15. Wen, J.G.; Xiao, Q.; Yang, Y.P.; Liu, Q.H.; Zhou, Y. Remote sensing estimation of aquatic chlorophyll-a concentration based on Hyperion data in Lake Taihu. *J. Lake Sci.* **2006**, *18*, 327–336. (In Chinese)
16. Wang, S.S.; Li, Y.M.; Wang, Y.B.; Wang, S.; Du, C.G. Suitability of the retrieval models for estimating chlorophyll concentration in Lake Taihu. *J. Lake Sci.* **2015**, *27*, 150–162. (In Chinese)
17. Huang, C.C.; Wang, X.L.; Yang, H.; Li, Y.M.; Wang, Y.H.; Chen, X.; Xu, L.J. Satellite data regarding the eutrophication response to human activities in the plateau lake Dianchi in China from 1974 to 2009. *Sci. Total Environ.* **2014**, *485–486*, 1–11. [CrossRef]
18. O'Reilly, J.E.; Maritorena, S.; Siegel, D.A.; O'Brien, M.C.; Toole, D.; Mitchell, B.G.; Kahru, M.; Chavez, F.P.; Strutton, P.; Cota, C.F.; et al. *SeaWiFS Postlaunch Calibration and Validation Analyses*; Part 3; NASA Tech; NASA Goddard Space Flight Center: Greenbelt, MD, USA, 2000; p. 49.
19. Gurlin, D.; Gitelson, A.A.; Moses, W.J. Remote estimation of chl-a concentration in turbid productive waters—return to a simple two-band NIR-red model? *Remote Sens. Environ.* **2011**, *115*, 3479–3490. [CrossRef]
20. Matthews, M.W.; Bernard, S.; Robertson, L. An algorithm for detecting trophic status (chlorophyll-a), cyanobacterial-dominance, surface scums and floating vegetation in inland and coastal waters. *Remote Sens. Environ.* **2012**, *124*, 637–652. [CrossRef]
21. Liu, G.; Li, L.; Song, K.S.; Li, Y.M.; Lyu, H.; Wen, Z.D.; Fang, C.; Bi, S.; Sun, X.P.; Wang, Z.M. An OLCI-based algorithm for semi-empirically partitioning absorption coefficient and estimating chlorophyll a concentration in various turbid case-2 waters. *Remote Sens. Environ.* **2020**, *239*, 1–26. [CrossRef]
22. Ioannou, I.; Gilerson, A.; Gross, B.; Moshary, F.; Ahmed, S. Deriving ocean color products using neural networks. *Remote Sens. Environ.* **2013**, *134*, 78–91. [CrossRef]
23. Italian Space Agency. The Satellite of the Italian Space Agency Launched from the European Base of Korou Aboard a Vega Launcher. Available online: https://www.asi.it (accessed on 7 November 2020).
24. Alonso, K.; Bachmann, M.; Burch, K.; Carmona, E.; Cerra, D.; Reyes, R.D.L.; Dietrich, D.; Heiden, U.; Hölderlin, A.; Ickes, J.; et al. Data Products, Quality and Validation of the DLR Earth Sensing Imaging Spectrometer (DESIS). *Sensors* **2019**, *19*, 4471. [CrossRef]

25. Zhuhai Orbita Aerospace Technology Co., Ltd. The Registration System of Orbita Hyperspectral Competition. Basic Information of Zhuhai No. 1 OHS Hyperspectral Satellite. Available online: https://ohs.obtdata.com/#/newsDetail?id=9 (accessed on 30 May 2019).
26. Deng, S.B.; Chen, Q.J.; Du, H.J.; Xu, E.H. *ENVI Remote Sensing Image Processing Method*, 2nd ed.; Higher Education Press: Beijing, China, 2014; pp. 277–324. (In Chinese)
27. Liu, D.; Pan, D.; Bai, Y.; He, X.; Wang, D.; Wei, J.A.; Zhang, L. Remote sensing observation of particulate organic carbon in the Pearl River estuary. *Remote Sens.* **2015**, *7*, 8683–8704. [CrossRef]
28. Mueller, J.L.; Morel, A.; Frouin, R.; Davis, C.; Arnone, R.; Carder, K. *Ocean Optics Protocols for Satellite Ocean Color Sensor Validation. Radiometric Measurements and Data Analysis Protocols*, 3rd ed.; NASA Goddard Space Flight Center: Greenbelt, MD, USA, 2003; pp. 1–63.
29. Morel, A.; Mueller, J.L. Normalized Water-Leaving Radiance and Remote Sensing Reflectance: Bidirectional Reflectance and Other Factors. Available online: http://ntrs.nasa.gov/archive/nasa/casi.ntrs.nasa.gov/20020044099.pdf#page=54 (accessed on 18 June 2020).
30. Mobley, C.D. Estimation of the remote-sensing reflectance from above-surface measurements. *Appl. Opt.* **1999**, *38*, 7442–7455. [CrossRef]
31. Tang, J.W.; Tian, G.L.; Wang, X.Y.; Wang, X.M.; Song, Q.J. The methods of water spectra measurement and analysis I: Above-water method. *J. Remote Sens. Beijing* **2004**, *8*, 37–44. (In Chinese)
32. Shi, K.; Zhang, Y.; Zhou, Y.; Liu, X.; Zhu, G.; Qin, B.; Gao, G. Long-term MODIS observations of cyanobacterial dynamics in Lake Taihu: Responses to nutrient enrichment and meteorological factors. *Sci. Rep.* **2017**, *7*, 40326. [CrossRef]
33. American Public Health Association; American Water Works Association; Water Environment Federation. *Standard Methods for the Examination of Water and Wastewater*; American Public Health Association: Washington, DC, USA, 1998; pp. 1–40.
34. Huang, X. *Eco-Investigation. Observation and Analysis of Lakes*; Standard Press of China: Beijing, China, 1999. (In Chinese)
35. Zheng, Z.B.; Li, Y.M.; Guo, Y.L.; Xu, Y.F.; Liu, G.; Du, C.G. Landsat-Based Long-Term Monitoring of Total Suspended Matter Concentration Pattern Change in the Wet Season for Dongting Lake, China. *Remote Sens.* **2015**, *7*, 13975–13999. [CrossRef]
36. Sun, D.Y.; Li, Y.M.; Wang, Q.; Lyu, H.; Le, C.F.; Huang, C.C.; Gong, S.Q. Detection of suspended-matter concentrations in the shallow subtropical Lake Taihu, China, using the SVR model based on DSFS. *IEEE Geosci. Remote Sens.* **2010**, *7*, 816–820. [CrossRef]
37. Zhu, B.; Wang, X.H.; Tang, L.L.; Li, C.R. Review on Methods for SNR Estimation of Optical Remote Sensing Imagery. *Remote Sens. Technol. Appl.* **2010**, *25*, 303–309. (In Chinese)
38. Wang, X.W.; Wang, C.X.; Zhang, Y.Y.; Li, C.R. Research on SNR of Point Target Image. *Electron. Opt. Control.* **2010**, *17*, 18–21. (In Chinese)
39. Neil, C.; Spyrakos, E.; Hunter, P.D.; Tyler, A.N. A global approach for chlorophyll-a retrieval across optically complex inland waters based on optical water types. *Remote Sens. Environ.* **2019**, *229*, 159–178. [CrossRef]
40. Liu, G.; Simis, S.G.H.; Li, L.; Wang, Q.; Li, Y.M.; Song, K.S.; Lyu, H.; Zheng, Z.B.; Shi, K. A Four-Band Semi-Analytical Model for Estimating Phycocyanin in Inland Waters from Simulated MERIS and OLCI Data. *IEEE Geosci. Remote Sens.* **2017**, *56*, 1374–1385. [CrossRef]
41. Sun, D.Y.; Hu, C.M.; Qiu, Z.F.; Shi, K. Estimating phycocyanin pigment concentration in productive inland waters using Landsat measurements: A case study in Lake Dianchi. *Opt. Express* **2015**, *23*, 3055–3074. [CrossRef]
42. Ruddick, K.G.; Gons, H.J.; Rijkeboer, M.; Tilstone, G. Optical remote sensing of chlorophyll-a in case 2 waters by use of an adaptive two-band algorithm with optimal error properties. *Appl. Opt.* **2001**, *40*, 3575–3585. [CrossRef] [PubMed]
43. Dall'Olmo, G.; Gitelson, A.A. Effect of bio-optical parameter variability on the remote estimation of chlorophyll-a concentration in turbid productive waters: Experimental results. *Appl. Opt.* **2005**, *44*, 412–422. [CrossRef] [PubMed]
44. Le, C.F.; Li, Y.M.; Zha, Y.; Sun, D.Y.; Huang, C.C.; Lu, H. A four-band semi-analytical model for estimating chlorophyll a in highly turbid lakes: The case of Taihu Lake, China. *Remote Sens. Environ.* **2009**, *113*, 1175–1182. [CrossRef]
45. Neville, R.A.; Gower, J.F.R. Passive remote sensing of phytoplankton via chlorophyll a fluorescence. *J. Geophys. Res.* **1977**, *82*, 3487–3493. [CrossRef]
46. Li, J.; Chen, X.L.; Tian, L.Q.; Huang, J.; Feng, L. Improved capabilities of the Chinese high-resolution remote sensing satellite GF-1 for monitoring suspended particulate matter (SPM) in inland waters: Radiometric and spatial considerations. *J. Photogramm. Remote Sens.* **2015**, *106*, 145–156. [CrossRef]
47. Bi, S.; Li, Y.M.; Lyu, H.; Zhu, L.; Mou, M.; Lei, S.H.; Xu, J.; Wen, S.; Ding, X.L. Estimation of chlorophyll-a concentration in Lake Erhai based on OLCI data. *J. Lake Sci.* **2018**, *30*, 701–712. (In Chinese) [CrossRef]
48. Yang, W.; Matsushita, B.K.; Chen, J.; Fukushima, T.; Ma, R.H. An Enhanced Three-Band Index for Estimating Chlorophyll-a in Turbid Case-II Waters: Case Studies of Lake Kasumigaura, Japan, and Lake Dianchi, China. *IEEE Geosci. Remote Sens.* **2010**, *7*, 655–659. [CrossRef]
49. Guo, Y.L.; Li, Y.M.; Li, Y.; Lyu, H.; Liu, G.; Wang, X.D.; Zhang, S.M. A Three Band Chlorophyll-a Concentration Estimation Model Based on GOCI Imagery. *J. Environ. Sci. China* **2015**, *36*, 3175–3185. [CrossRef]
50. Härmä, P.; Vepsäläinen, J.; Zha, Y.; Hannonen, T.; Pyhälahti, T.; Kämäri, J.; Kallio, K.; Eloheimo, K.; Koponen, S. Detection of water quality using simulated satellite data and semi-empirical algorithms in Finland. *Remote Sens. Environ.* **2001**, *268*, 107–121. [CrossRef]

51. Du, C.; Wang, S.X.; Zhou, Y.; Yan, F.L. Remote chlorophyll a retrieval in Taihu Lake by three-band model using Hyperion hyperspectral data. *J. Environ. Sci. China* **2009**, *30*, 2904–2910.
52. Lyu, H.; Li, X.J.; Wang, Y.N.; Jin, Q.; Cao, K.; Wang, Q.; Li, Y.M. Evaluation of chlorophyll-a retrieval algorithms based on MERIS bands for optically varying eutrophic inland lakes. *Sci. Total Environ.* **2015**, *530–531*, 373–382. [CrossRef] [PubMed]